(3)

Dynamics Technology, Inc.

DT 8723-01

Laboratory Feasibility Study Of A Composite Embedded Fiber Optic Sensor For Measurement of Structural Vibrations

February, 1988

By: C. Michael Dube, Dynamics Technology, Inc.

Tom D. Wang, Dynamics Technology, Inc.

Robert G. Melton, Pennsylvania State University, Department of Aerospace Engineering

David W. Jenson, Pennsylvania State University, Department of Aerospace Engineering

Mike Koharchik, Pennsylvania State University, Department of Aerospace Engineering

Dynamics Technology, Inc.
21311 Hawthorne Blvd., Suite 300
Torrance, Ca. 90505
(213) 543-5433

TABLE OF CONTENTS

PROJECT SUMMARY

Dynamics Technology, Inc. (DTI) and the Pennsylvania State University (PSU) Department of Aerospace Engineering have assessed the feasibility of using fiber optic strain sensors embedded in a composite material to measure the magnitude and frequency of structural vibrations for control of flexible elements. The objectives of this Phase I study were to demonstrate the ability to embed fiber optic strain sensors in a composite material, to determine the performance of these sensors, to identify active control system architectures that are matched to the fiber optic system measurands to damp vibrations of large space structures, and to estimate the stability achievable by these methods.

A detailed laboratory study was performed in which DTI built a wide band closed-loop-fiber Mach-Zehnder interferometer to conduct transverse vibration measurements on sub-scale composite elements with embedded fiber sensors, which were fabricated by PSU. The interferometer detects vibrations by measuring the strain transferred by the composite to the embedded optical fiber. The strain sensor demonstrated the ability to track the vibrations of a cantilever beam over a frequency bandwith ranging from approximately 5 Hz to almost 1000 Hz. The sensor was unable to detect dc strains because of thermal drift and laser power fluctuations. These factors produced a drift in the dc signal level, which was indistinguishable from static strain measurements. Beyond 1000 Hz, the composite element was unable to follow the drive mechanism. The noise equivalent strain was $\epsilon \simeq 10^{-10}$.

Analysis has been conducted on the control of structural shape of large space structures. General design principles are applied to the specific case of a cantilever beam, as a representative structural member. The control concepts focus on the positioning of the free end of the beam. The control issues are then extended to arbitrary structural shapes.

The concept of embedded fiber sensors has been clearly demonstrated in the Phase I project and an approach for an integrated structural control system has been identified. The principal issues to be addressed in Phase II are:

- Refinement of the fiber configuration within the composite element to enhance the sensor response at higher frequencies and for torsional as well as bending modes.
- Investigation of techniques to measure near-dc structural deflections.
- Development of fiber sensor combinations or adaptation of multiplexing techniques suitable to structural subgroups.
- Implementation of a prototype control algorithm matched to the signal characteristics of distributed fiber optic sensors.
- Demonstration of a small scale, end-to-end structural vibration control system which can be used to identify engineering issues and to validate system concepts.

FOREWORD

This program was conducted under contract SDIO 87-12. The work was funded through the Small Business Innovative Research Program (SBIR) and performed from October 1987 through February 1988. The technical monitor for this work was Dr. Albert Tucker of the Office of Naval Research. Technical discussions with Dr. Keith Wanser of Dynamics Technology, Inc. are greatly appreciated.

1. INTRODUCTION

Control of flexible space structures is a problem that extends to several initiatives in the development of orbiting platforms. In particular, SDI platforms will require a very high degree of pointing accuracy and stability, $\sim 10^{-6}$ radians. A number of ventures involving large satellites and other strategic defense platforms, such as Spaced Based Laser and Space Based Radar, will employ designs that incorporate flexible appendages, such as lightweight mirrors and antennas, whose operation depends upon a carefully controlled microgravity environment, i.e. minimal accelerations. Pointing accuracy must be maintained in the presence of self-induced platform motion (tracking and retargetting) and impact from foreign objects.

Future space structures will make abundant use of composite laminates using advanced resins reinforced with high stiffness materials, such as graphite and boron. To minimize the problems associated with vibration of these large, lightweight structures, new concepts in active control are needed. A critical element of such a control system is an integrated measurement system that will sense the state of deformation or strain with adequate bandwidth to resolve and null the energetic vibration modes.

Dynamics Technology, Inc (DTI) and Pennsylvania State University (PSU) Department of Aerospace Engineering propose a technique for vibration control that uses embedded fiber optic sensors and an integrated control system to measure the distributed strain in structural elements and provide active feedback for force transducers. Fiber optic sensors have been shown to offer unique advantages in sensing strain, temperature, and other quantities in harsh environments. The state of strain of a structural element with embedded fibers can be sensed over a broad area of the structure, since the optical fibers are laid up in the structure along with the composite fibers. The necessary control-related measurements can be made continuously while the structure is undergoing a vibrational excitation. Potential advantages of fiber optic strain sensors embedded in composite materials include:

- Structural advantages of composites plus potential for rugged embedded sensors through laminated fabrication techniques.
- High resolution, wide bandwidth, low power consumption, EMI resistance, and flexible geometry possible with fiber optic sensors.
- Synergism of fiber optic sensors and advanced control theory to achieve an integrated structural control system.
- Possibility of efficient optical signal processing of data from numerous sensors in a large scale advanced system.

The goal of this SBIR research program is to demonstrate the feasibility of building a composite-embedded, fiber optic sensor, active, structural control system for strategic defense platforms. The specific Phase I objectives were the following:

- Demonstrate feasibility of embedding fiber optic strain sensors in a composite material in the laboratory.

- Characterize the baseline performance of embedded fiber optic sensors.

- Identify candidate active control techniques, algorithms and associated distributed sensor geometries for control of large space structures.

- Estimate the stability achievable by the candidate techniques.

The results of this Phase I study confirm the viability of a fiber optic strain sensor to detect and measure low amplitude composite element vibrations. The fiber optic strain sensor was successfully embedded within the sub-scale composite element and measurements of the induced vibrations using the interferometric sensors followed the response predicted by theory with good accuracy. Also, control analysis was performed on methods to constrain the vibrations.

A description of the embedded fiber optic sensor experiment and theory is discussed in Section 2, followed by the results of the lab tests in Section 3. Section 4 consists of the analysis of the candidate active control methods. A summary of the requirements for the Phase II development is included in Section 5.

2. SYSTEM DESIGN APPROACH

The experimental aspects of this study involved building the fiber interferometer, developing the electronic circuitry, and fabricating the composites with embedded fiber. The embedded sensor system consists of two major design elements: (1) a closed-loop, wideband, fiber optic interferometer and (2) a fiber-embedded composite structural element.

2.1 Fiber Optic Interferometer Design

The vibration sensing system is built around a fiber optic Mach-Zehnder interferometer, as shown in Fig. 2.1. A HeNe laser directs light through a 125 micron diameter fiber and the incident light is split into two legs by an integrated fiber optic directional coupler. One leg contains the transducer element (in this case the fiber embedded composite element) and the other is a static reference leg. The coupler is ruggedized to insure constant coupling amidst temperature variations. The output intensity is detected by a pair of photodiodes, and any shift in the relative phase of the light in the two legs is sensed as an intensity change at the photodiodes. A piezoelectric (PZT) cylinder wound with optical fiber acts as a strain compensation element, and is used in an active feedback loop to maintain the interferometer in "quadrature" ($\pi/2$ relative phase), where it has maximum sensitivity, as shown in Fig. 2.2.

In general, the light output of a fiber interferometer can be split in any proportion between the two output fibers depending on the relative phase at the output coupler. The interferometer is most sensitive to small phase changes when the relative phase between the two optical legs is π, $3\pi/2$, and so on, as shown in Fig. 2.2. Usually, slow ambient temperature variations will cause a drift in the relative output phase due to small differential strains in the two interferometer legs. The PZT's in the compensation system have linear voltage-expansion coefficients and are used in feedback loop to strain the fiber in the reference leg until quadrature is attained.

For efficient interferometric coupling, or optimum constructive and destructive interference, the light in each leg should have about the same polarization direction at the output coupler. Although the light output of a laser may be highly polarized, birefringence in single mode fibers significantly alters this polarization. Differences in polarization result in a reduction of the fringe visibility. Drifting of the polarization with time will change the fringe visibility and the phase sensitivity of the device.

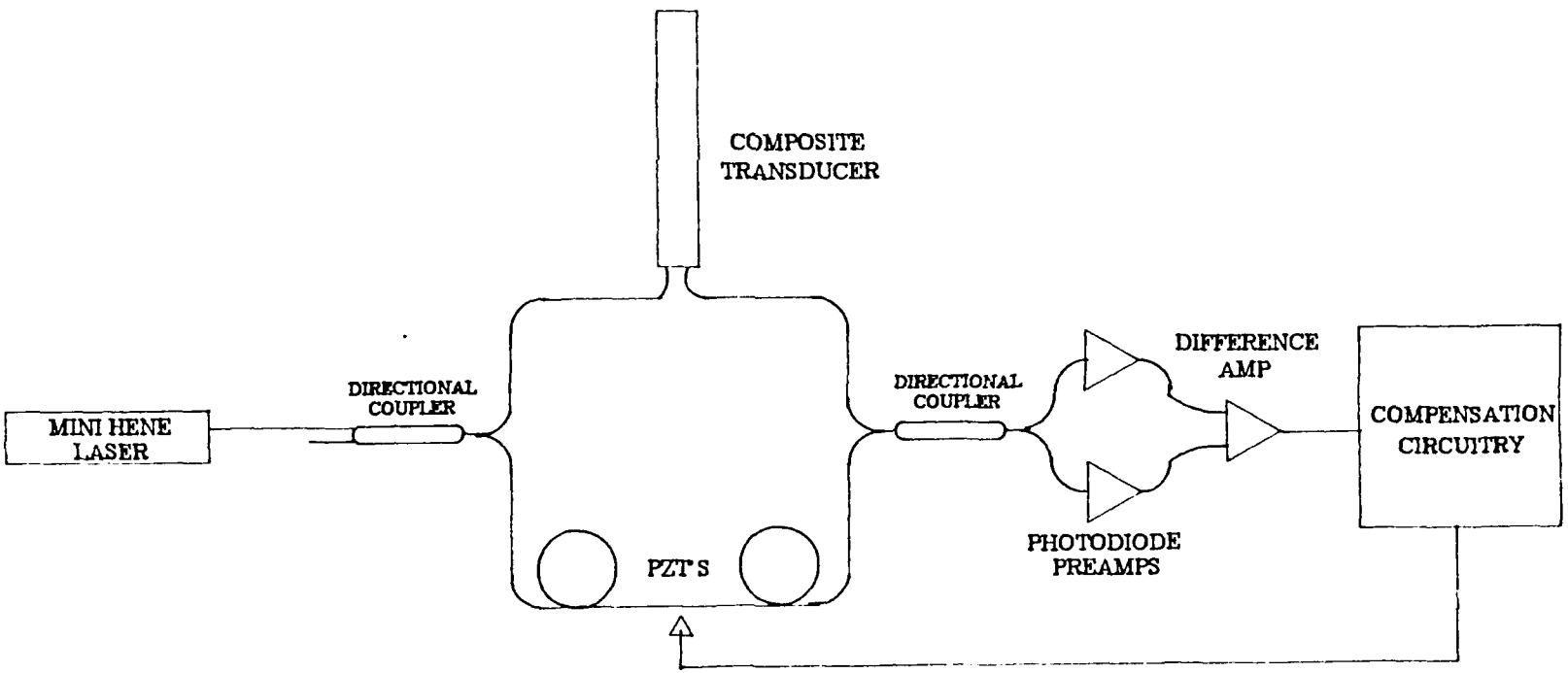

Fig. 2.1 Dual Feedback Stabilized Mach-Zehnder Interferometer

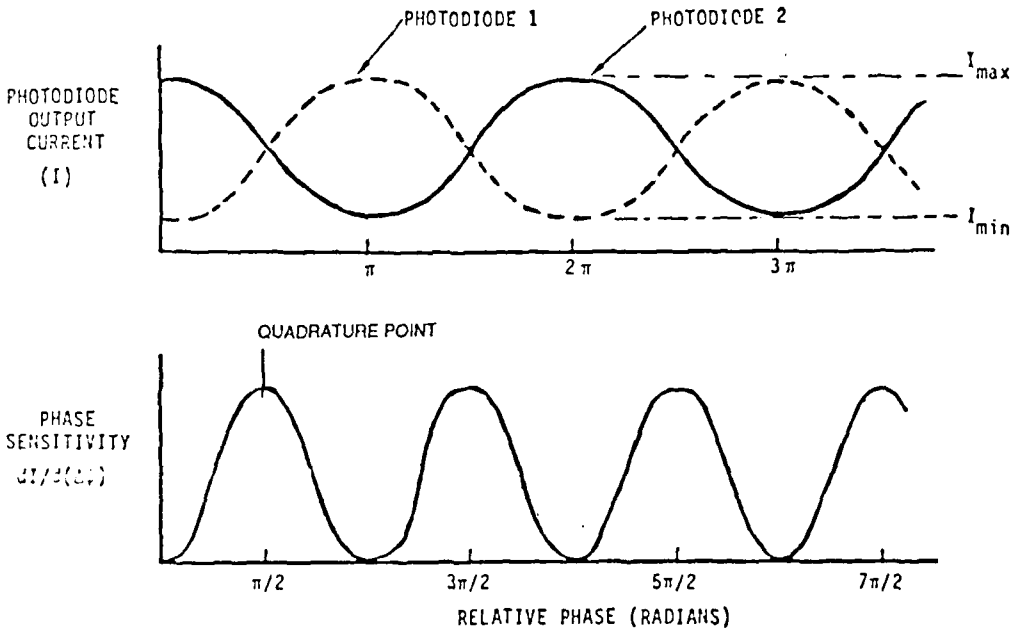

Fig. 2.2 Interferometer Phase Sensitivity

In order to minimize the polarization drift problem, a phase detection scheme was used that minimizes the polarization drift effect with a fast quadrature tracking feedback loop that keeps the photodiode output levels equal regardless of the fringe visibility. In this scheme, an optical error signal generated in the interferometer by either signal or noise is filtered, integrated, and then fed back to the fiber wound PZT, keeping the interferometer balanced. The integrated error signal is then a linear measure of the optical phase shift to be evaluated.

The calibration of optical phase shift depends only on the fixed PZT strain constant of the feedback element. The radian/volt conversion was measured to be 3.6 rad/V. It is nominally insensitive to polarization drift which affects fringe visibility. In this configuration, the principal effect of polarization drift is to partially reduce the sensor bandwidth which is a problem that can be largely overcome by conservative design of the feedback bandwidth.

An important constraint in the circuit design is the need to prevent the fundamental mechanical resonance of the piezoelectric element from causing loop instability. The PZT resonant frequency for the experimental set-up occurs at about 30 kHz and high frequency noise can excite the PZT elements and alter the performance. The resonance problem can be managed by adjusting the gain on the PZT feedback amplifier following classical control loop design principles.

2.2 **Composite Sensor Design and Fabrication**

As indicated in the introduction, the flexibility of optical fiber permits a countless array of configurations for distributed strain measurements. By appropriate choice of fiber routing, one may extract linear strain, bending, torsion, differential strain, or combinations of these. Similarly, by concentrating more fiber in areas of particular interest (e.g. vibrational nodes or edges) one may amplify the contribution from these areas to the total integrated strain output.

Because of the limited scope of Phase I and the desire to demonstrate conceptual feasibility and consistency with readily obtainable theoretical predictions, a relatively simple fiber/structural configuration was chosen consisting of a rectangular beam with the embedded fiber offset uniformly form the axis of symmetry. This configuration was made to avoid having any fiber protrude out from the free end of the composite since loose fiber in the vibration tests would add unnecessary noise to the measurements. Obviously, more complex structures would be the focus of Phase II.

The procedure used in the fabrication of the test specimens was as follows. Twenty plies of 640-600/5245C graphite/epoxy prepreg were cut and laid up in the prescribed $[0_4/90]_s^2$ layup. After the 18th ply was layed, a length of optical fiber was cut and layed on the ply in the configuration shown in Figure 2.3a. The remaining two plies were then layed onto the specimen. Pigtails approximately one meter in length were left on the optical fiber to facilitate splicing into the interferometer. The specimen was then cured in a programmable hot press using the manufacturer's suggested cure cycle. A pressure of 100 psi was applied throughout the cycle. The temperature was raised at 2°F/min. to 350°F and held for 2 hours. Finally, the temperature was decreased at 5°F/min. to 90°F. The specimen was then removed and cut to size with a diamond impregnated saw.

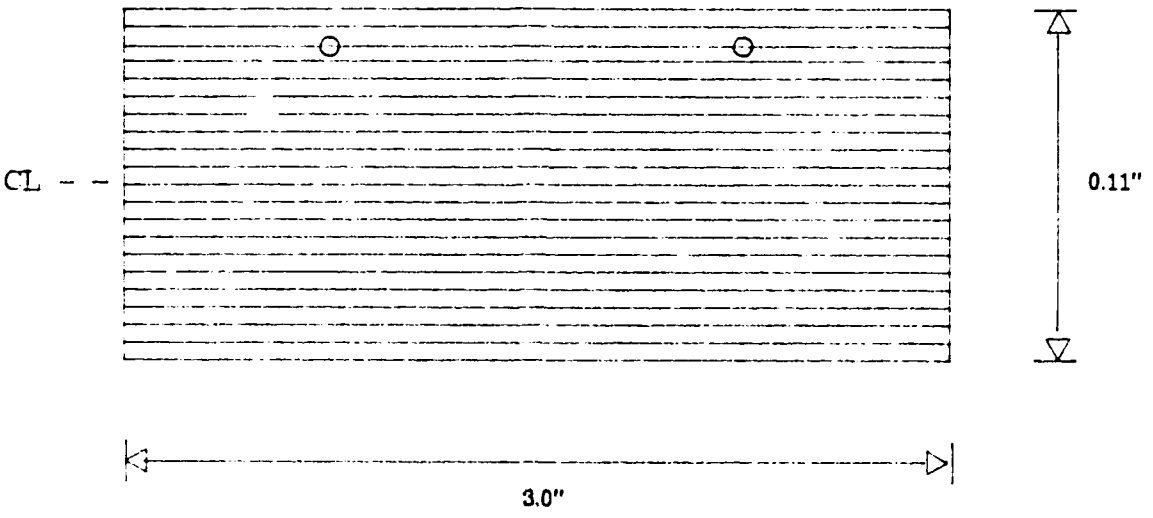

Fig. 2.3a
The composite sample with embedded fiber optic contains twenty plies. The fiber optic is laid between the 8th and 9th ply up from the center line (CL).

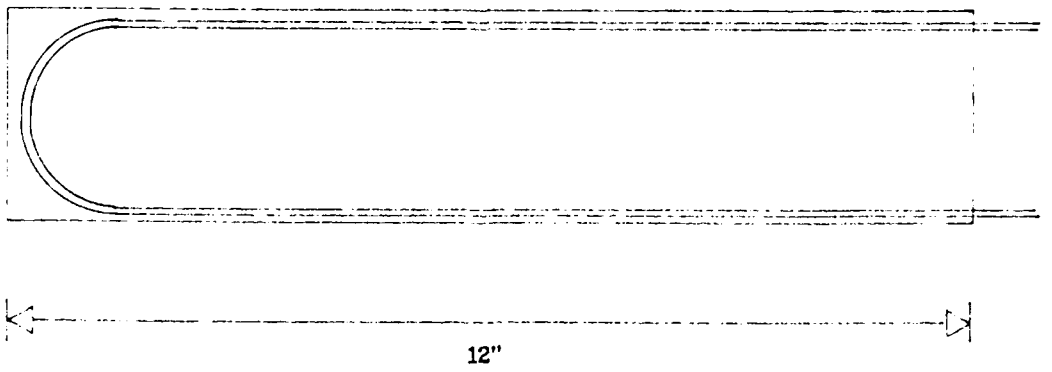

Fig. 2.3b
The fiber optics is laid from one end back around to prevent protrusion of the fiber on one end. This arrangement avoids noise pick up from loose fiber.

3. LABORATORY TESTS

Single mode optical fiber was successfully embedded in a sub-scale composite sample, and was spliced into the transducer leg of the interferometer strain sensor. The performance of the subscale demonstration sensor was evaluated by driving the composite element at various frequencies and amplitudes and observing the sensor's response. A comparison was made of the actual displacement of the free end of the cantilever with the value predicted from theory using the interferometer output data. The free end displacement was measured by a mechanical displacement gauge or a laser reflection device, and the measurements are accurate to within ±0.005 inches.

The Mach-Zehnder interferometer described in Section 2.1 was used to detect the vibrations by measuring the strain transferred by the composite cantilever to the embedded optical fiber. Thus, as the cantilever bends during vibration, the fiber will experience tension and compression. This change in length of the transducer leg of the interferometer causes a phase difference in the laser light relative to that in the reference leg. An electronic circuit is then used to produce a voltage proportional to the magnitude and frequency of the light phase shift which is approximately proportional to the change in fiber length.

In the experiment the composite was arranged as a cantilever with one end fixed and the other left free to vibrate. This geometry was convenient to produce forced oscillations and provided for a straightforward solution to the equation of motion. The vibration analysis, discussed in Appendix B, was done by modeling the composite as a homogeneous beam with continuously distributed mass and elasticity, which was shown to be a good approximation. The experiments revealed results consistent with the theoretical analysis of cantilever beam vibration. The sensor was able to response drive frequencies from 5 to 1000 Hz with vibration amplitudes as high as 0.5 mm for a 10.5" long cantilever at its resonance and a noise equivalent stain of 10^{-10}. The bandwith of the response is limited on the upper end by the ability of the composite element to follow the drive frequency. The amplitude of the response is limited by the power supply voltages and the radian/volt scale factor of the PZT. The circuit was designed to reset at a peak voltage of 10V and the scale factor of 3.6 rad/volt allowed for maximum fiber elongation amplitudes of 36 radians.

3.1 Test Set-Up

The experimental tests were conducted in two parts. First, at DTI, a simple arrangement was set-up with the composite element clamped on one end to the edge of a table. A razor blade, used for its ferrous content, was glued to the free end of the composite. An electromagnet was then used to the cantilever. The set-up was used to demonstrate the operation of the interferometer and to validate the cantilever vibration modeling assumptions.

A more sophisticated approach was undertaken at PSU where the composite element was driven with a mechanical shaker as shown in Figs. 3.1 and 3.2. The shaker has a flat response over the frequency range which the composite could follow the drive, which was about 1 kHz. The displacement of the cantilever beam was measured with the dial gauges shown in Fig. 3.2 with an accuracy of ±.005 inches. A close-up view of the bench top fiber optic inteferometer is shown in Fig. 3.3.

3.2 **Identification of Natural Frequencies**

At DTI, measurements of the vibration amplitudes were taken over a sweep of frequencies to locate the resonance values. These resonant frequencies could be compared to the theoretical values, discussed in Appendix B, to the modeling assumptions. The response of the vibration sensor to a sinusoidal input was measured with cantilevers of lengths 4", 6", and 7". The resonances were located by identifying the voltage response maxima.

The first two natural frequencies predicted from theory for cantilevers of lengths 4", 6", and 7" are given below along with the measured first two resonant frequencies.

Table 3.1 Resonant Frequencies of Composite Element

Cantilever Length	Order of Mode	Theoretical	Experimental
4"	f_1	117 Hz	100 Hz
	f_2	732 Hz	----
6"	f_1	52 Hz	55 Hz
	f_2	236 Hz	----
7"	f_1	38 Hz	38 Hz
	f_2	239 Hz	230 Hz

The experimental results reasonably agree with the theory, hence the assumptions made to model the composite beam appear to be reasonable. The composite element failed to follow the simple magnetic drive beyond 300 Hz. Thus no data was obtained for the second harmonic for L=4" and L=6".

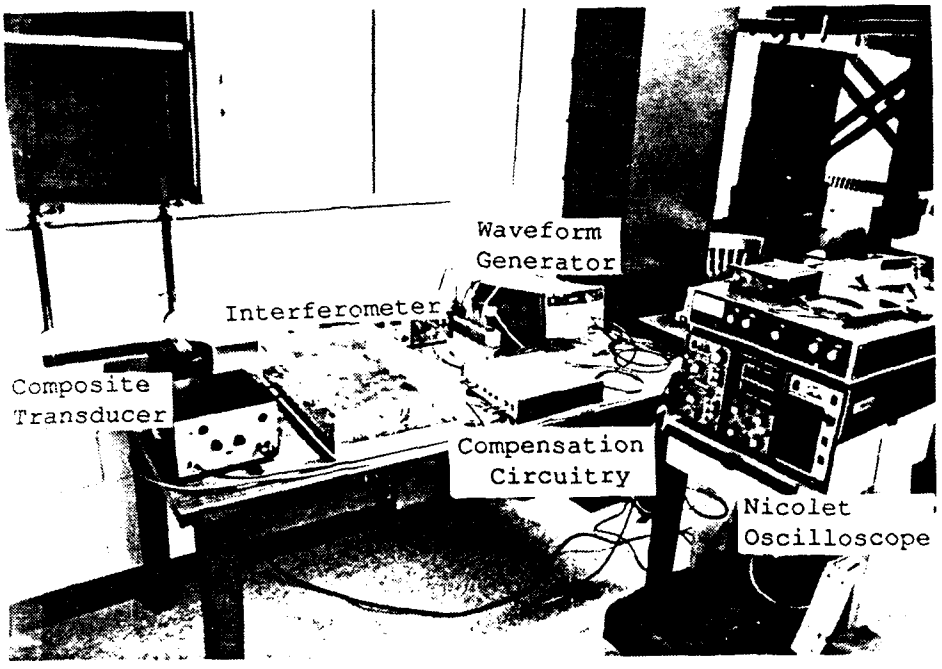

Fig. 3.1 Fiber Optic Strain Sensor
Set-up at Pennsylvania State University

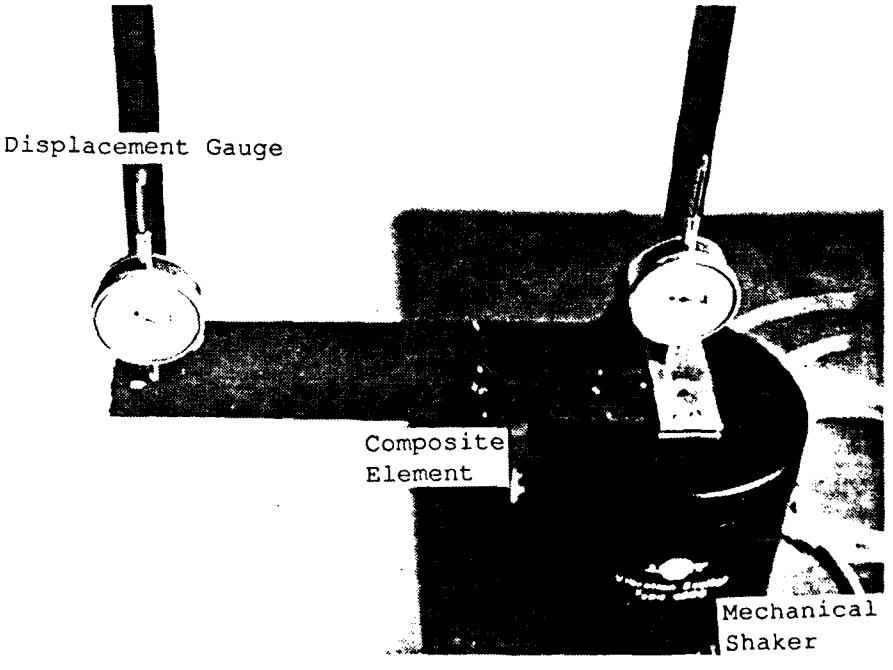

Fig. 3.2 Composite Element Driven By Mechanical
Shaker with Displacement Gauges.

Fig. 3.3 Bench Top Fiber Optic Interferometer

3.3 **Cantilever Impulse Response**

The second experiment performed at PSU, consisted of applying an impulse to the cantilever, and measuring the response. Fig. 3.4 shows a representative result. The upper trace is the beam's impulse response for which the amplitude initially rises to a maximum and then damps out. The lower trace is the impulse input. The cantilever length was set L=10.5, and the first three natural frequencies are 29 Hz, 187 Hz, and 578 Hz.

An impulse is a realistic perturbation to a space structure (e.g. impact of a foreign object), and its frequency response identifies the magnitude of the excited modes. A spectrum was computed of the cantilever's input response and is shown in Fig. 3.5. There are frequency peaks shown at 29 Hz, 50 Hz, 85 Hz, 150 Hz, 180 Hz, and 270 Hz. There are three frequencies excited in addition to the natural frequencies. There are three possible reasons for this discrepancy. First, the 270 Hz observed "natural" frequency may represent a subharmonic of the 580 Hz cantilever natural frequency. Second, the fibers extending from the base of the plate to the interferometer could have been excited since the base of the plate was being driven by the electromagnetic shaker. Thus, this extraneous frequency may actually represent a natural frequency of the optical cables. In any case, additional testing would need to be performed to positively identify the source of these extraneous modes. The large amplitude at 50 Hz is present because the impulse wavetrain was set at 50 Hz.

As previously mentioned, the existence of non-harmonic frequency peaks could be indicative of natural frequencies of other parts of the system, such as the electronics, the PZT's, or the fiber-optic pigtails. In order to minimize the vibrations in the pigtails, they were taped to the stationary part of the shaker, a short distance from the root. Enough slack was left such that the beam motion would not draw them tight. In this configuration, resonant motion of these short lengths of the pigtails is a distinct possibility. It was demonstrated that bending of the fibers resulted in a response from the interferometer. Therefore, resonant bending of the fiber optic cables could cause resonant behavior at their natural frequencies. An interesting note is that 85 Hz and 270 Hz are in the proper ratios to be the second and third harmonics, possibly, of the fiber optical cables.

3.4 **Sensor Calibration**

A representative sample of the data is shown in Fig. 3.6 at the composite's first resonance at 29 Hz. The upper trace is the interferometer output as measured from the feedback voltage to the PZT. The peak-to-peak voltage is 11.2 V, which is close to the interferometer maximum of 12 V. The lower trace is the input to the mechanical shaker. There is a difference in phase between the input and the output of 180 degrees because the output signal is taken from the feedback voltage to the PZT. The feedback is negative in sign relative to the optical phase shift.

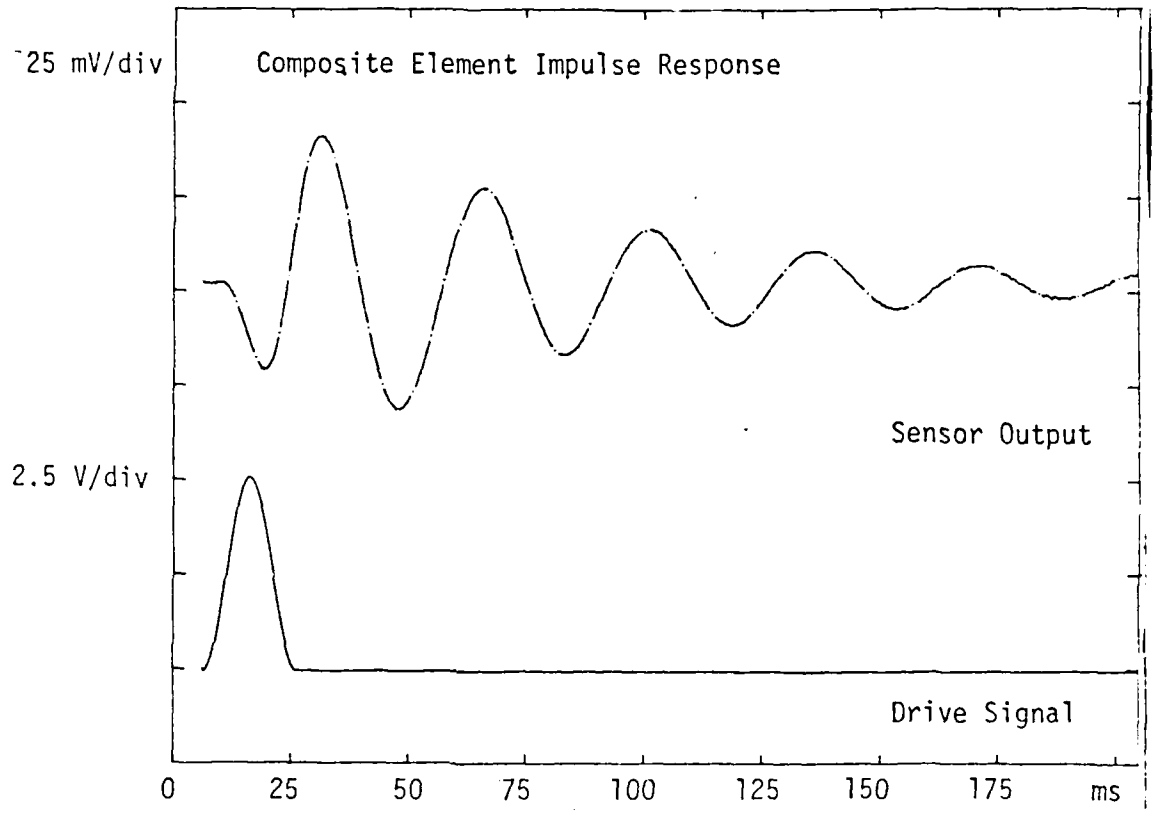

Figure 3.4 The upper trace is the response of the cantilever when excited with an impulse. The impulse signal, shown in the lower trace, is a realistic perturbation to a space structure.

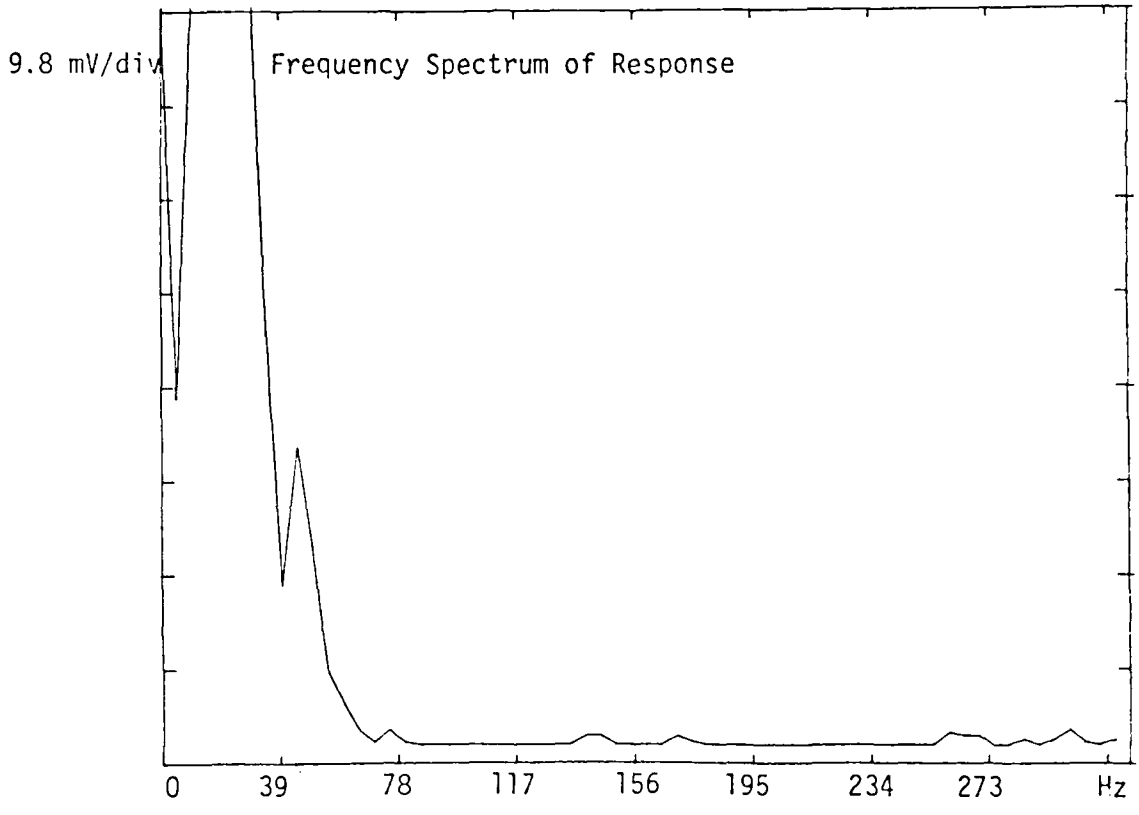

Figure 3.5 A spectrum is computed of the cantilever impulse response to determine the magnitudes of the excited frequency modes.

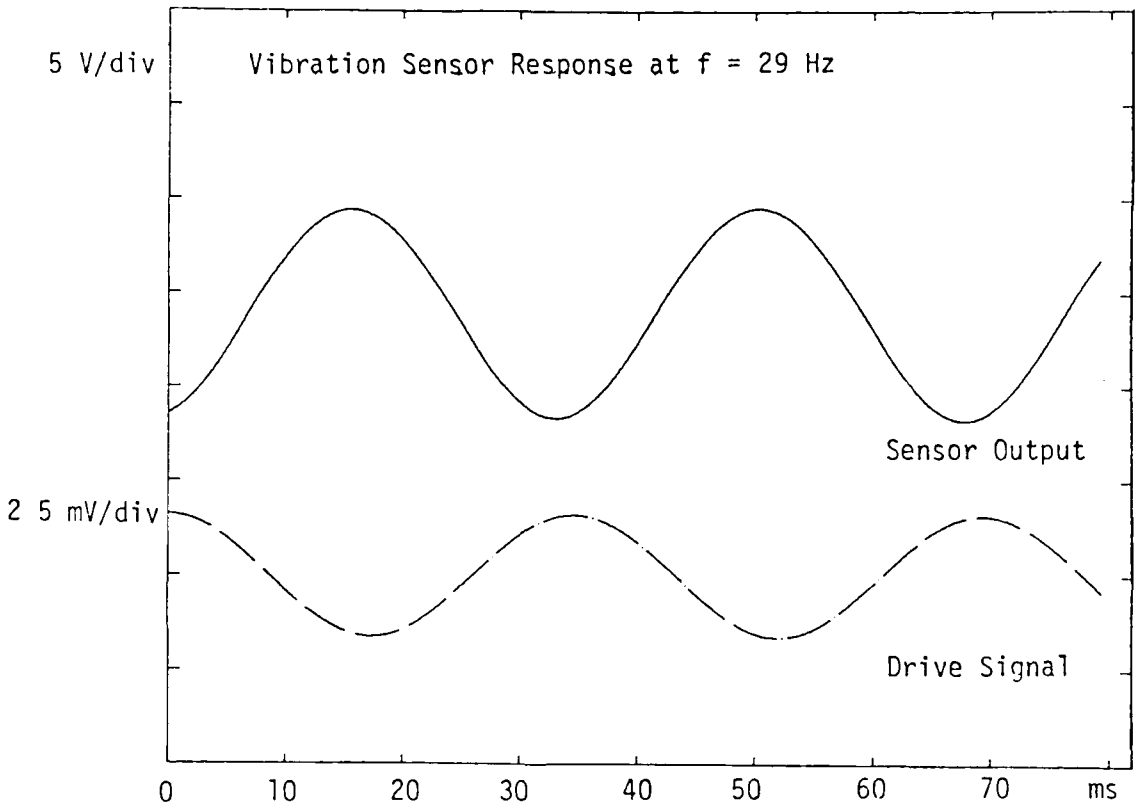

Figure 3.6 A representative sample of the data is shown at the composite's first resonance at 29 Hz. The upper trace is the sensor output as measured from the feedback voltage to the PZT. There is a difference in phase of 180 degrees, which is a result of the negative feedback feature.

The strain $\epsilon(x)$ at a distance x from the free end of the cantilever can be calculated from the free end displacement d from its equilibrium position. Equation 3.1 shows this relationship, and can be found in Reference 5.

$$\epsilon(x) = \frac{3dax}{L^3}, \tag{3.1}$$

where a is the distance from the neutral axis and L is the cantilever length.

The total elongation in the fiber can be found theoretically by integrating (3.1) from 0 to L and multiplying by 2 in order to account for the 2- pass fiber wrap in the composite element. The result is

$$\epsilon_T = \frac{3da}{L} \tag{3.2}$$

The measured end displacement d=.022 inches for the data shown in Fig. 3.6, corresponds to an elongation $\epsilon_T = 3\times10^{-6}$ m, or a maximum strain $\epsilon(L)=3\times10^{-5}$. The peak voltage of the sensor response is $V_p = 5.5V$, which, using the PZT scale factor of 3.6 rad/V, yields an experimentally measured elongation of $\epsilon_E = 2\times10^{-6}$ m. The theoretical and experimental values agree to the same order of magnitude. The discrepancy may be related to the use of (3.1), which has been derived for static strains. A spectrum of the interferometer noise was taken over the same frequency range as that of the vibration measurements, ~5 Hz to 1000 Hz. The broadband average noise was determined to be $\sim4\times10^{-4}$ $v/\sqrt{Hz}$. This value corresponds to a noise-equivalent strain on the orfer of magnitude of 10^{-10}, or a fiber elongation of $\epsilon_{noise} \approx 4\times10^{-11}$m.

The other data, presented in Appendix A, were taken for vibrational modes beyond the fundamental. No analytic equations were derived to relate the displacement to the strain for higher modes, thus, comparison of experimental measurements with theoretical predictions were not pursued.

In addition to the cantilever configuration in Fig. 2.3b, other sensor layouts were considered. One idea involved a double cantilever arrangement where the fiber protrude through the side of the composite, as shown in Fig. 3.7. However, succesful fabrication of this configuration had not been accomplished at the time of the test were conducted.

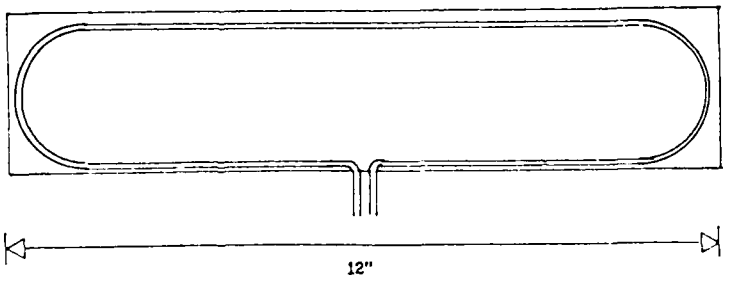

Fig. 3.7 Double cantilever arrangement of fiber in composite element.

4. VIBRATION CONTROL ANALYSIS

This section addresses the problem of controlling the structural shape of an element in a spacecraft. The form of control for a structure will depend strongly on exactly what is to be controlled (e.g., the position of one or more specific points on the surface of a structural member, or the overall shape of the member). Therefore, while general design methodologies for structural controllers are possible, ultimately, they must be applied in a manner appropriate to the specific structure under consideration and the specific performance criteria required of the controller. Accordingly, the analysis in Sections 4.1 and 4.2 examines the control concepts employed in this prototype control scheme are then conceptually extended to arbitrary structural shapes and embedded fiber sensors in Section 4.3.

4.1 Cantilevered Beam

Under the assumption of linear response, the differential equation of motion for a beam is

$$EI \frac{\partial^4 u(x,t)}{\partial x^4} + \rho \frac{\partial^2 u(x,t)}{\partial t^2} = F_c(x,t) \tag{1}$$

with a solution, in terms of modal components, of

$$u(x,t) = \sum_n A_n(t)\ \phi_n(x), \tag{2}$$

where
- E = modulus of elasticity
- I = area moment of interia
- ρ = mass per length of the beam
- uU = deflection of the beam
- F_c-(x,t) = control forcing function
- $A_n(t)$ = temporal part of the solution $u(x,t)$.
- $\phi_n(x)$ = mode shapes; i.e., spatial part of the solution.
- x = distance from fixed end of the cantilever beam
- t = time

For a cantilevered beam, the mode shapes are

$$\phi_n(x) = \left[\left(\frac{A}{B}\right)_n (\sinh\beta_n x - \sin\beta_n x) + \cosh\beta_n x - \cos\beta_n x \right], \tag{3}$$

with

$$\left(\frac{A}{B}\right)_n = \frac{-\cos\beta_n L + \cosh\beta_n L}{\sin\beta_n L + \sinh\beta_n L}, \tag{4}$$

where

L = length of beam

β_n = spatial frequencies, satisfying the characteristic equation:

$$(\cos\beta_n L)(\cosh\beta_n L) + 1 = 0 \quad \text{(See Appendix B and D)} \tag{5}$$

The general differential equation for the A_n is

$$\ddot{A}_n + \omega_n^2 A_n = f(t) \left[\frac{\int_o^L p(x)\phi_n(x)\, dx}{\rho \int_o^L \phi_n^2(x)\, dx} \right] \tag{6}$$

where

$$\omega_n = \frac{\beta_n^2}{L^2} \sqrt{\frac{EI}{\rho}} \tag{7}$$

= natural angular frequency corresponding to the n-th mode.

$p(x)$ = load factor (indicative of the force and moment distribution on the beam)

$(\cdot)$ = derivative with respect to time

and $F(t)$ = normalized time variation

If the control force is concentrated at location x_c, with strength F_o, then the external driving force (in this case, the control force) is

$$F_c = F_o \delta(x-x_c)\, f\text{-}(t) \tag{8}$$

where δ = Dirac delta function

and the numerator in the right-hand side of Equation (6) is then replaced with $F_o\phi_n(x_c)$

$$\ddot{A}_n + \omega_n^2 A_n = F_o\, f(t)\phi_n(x_c) \Big/ \rho \int_o^L \phi_n^2(x)\, dx \tag{9}$$

The displacement of the beam-tip (i.e. x = L) is determined using equation (2)

$$u(L,t) = \sum_n A_n \phi_n(L) \tag{10}$$

Now, taking Laplace transforms of equations (9) and 10) yields (transformed quantities are denoted by (~1)

$$\left[s^2 + \omega_n\right] \tilde{A}_n(s) = F_o \phi_n(x_c) F(s) \tag{11}$$

$$u(L,s) = \Sigma \tilde{A}_n(s) \phi_n(L) \tag{12}$$

from which a servo-control scheme can be devised, as shown in the block diagram below (Fig. 4.1):

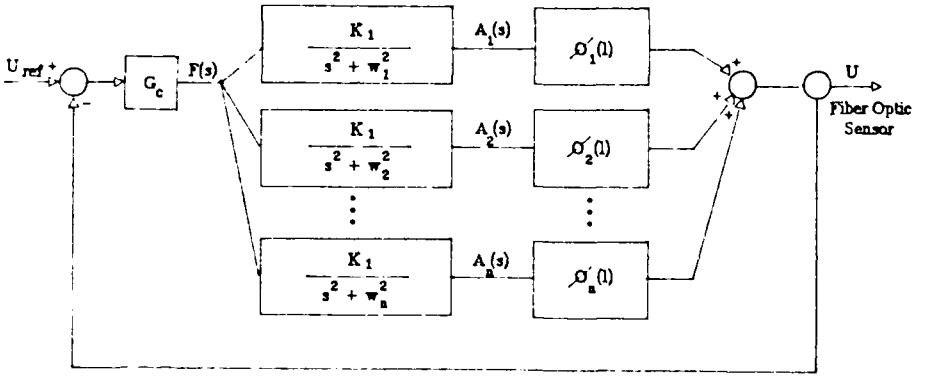

Fig. 4.1 The block diagram is shown fora servo-control scheme.

The quantity F(s) is the Laplace transform of the control force and U_{ref} in Fig. 4.1 is the desired (reference) value for u at the beam-tip. In order to realize this controller, the number of modes being modeled must be decided *a priori*, and their appropriate transfer functions inserted in the parallel group of blocks that generate the A_n values.

The G_c is a compensator, designed to give the desired characteristics for the controller. This design will depend strongly upon how many modes are to be controlled (i.e. how many of the K_n are retained in the system model). Note that the K_n are given by

$$K_n = \frac{F_o \phi_n(x_c)}{\rho \int_o^L \phi_n^2(x)\,dx}$$

where the integral in the denominator is

$$\int_0^L \phi^2(x)\,dx = \frac{\frac{\sin 2\beta_n L}{2} + \beta_n L}{2\beta_n} + \left(\frac{A}{B}\right)_n^2 \left\{ \frac{\beta_n L - \frac{\sin 2\beta_n L}{2}}{2\beta_n} \right.$$

$$- \frac{e^{-\beta_n L}}{2\beta_n}\left[\left(e^{2\beta_n L} + 1\right)\sin\beta_n L + \left(1 - e^{2\beta_n L}\right)\cos\beta_n L\right]$$

$$\left. + \frac{\frac{e^{2\beta_n L}}{2\beta_n} - \frac{e^{-2\beta_n L}}{2\beta_n} - 2L}{4} \right\}$$

$$- 2\left\{ \frac{e^{-\beta_n L}}{4\beta_n}\left[\left(e^{2\beta_n L} + 1\right)\sin\beta_n L + \left(e^{2\beta_n L} - 1\right)\cos\beta_n L\right] \right.$$

$$+ \left(\frac{A}{B}\right)_n \frac{e^{-\beta_n L}}{4\beta_n}\left[\left(e^{2\beta_n L} - 1\right)\sin\beta_n L + \left(e^{2\beta_n L} + 1\right)\cos\beta_n L\right]$$

$$\left. + \left(\frac{A}{B}\right)_n \frac{\cos^2\beta_n L}{2\beta_n} \right\}$$

$$+ 2\left(\frac{A}{B}\right)_n \left\{ \frac{\cosh^2\beta_n L}{2\beta_n} - \frac{e^{-\beta_n L}}{4\beta_n}\left[\left(e^{2\beta_n L} - 1\right)\sin\beta_n L + \left(e^{2\beta_n L} - 1\right)\cos\beta_n L\right] \right.$$

$$\left. + \left\{ \frac{e^{2\beta_n L}}{2\beta_n} - \frac{e^{-2\beta_n L}}{2\beta_n} + 2L \right\} \cdot \frac{1}{4} \right\}$$

4.2 Example Control System

As shown in Fig. 4.2 the control force is applied at position x_c. If U_{ref} (input to the controller) is 0, then the control loop will alter the control force as needed (in the presence of some disturbance), attempting to regulate the position of the beam-tip at zero-deflection. The sensing is performed by the fiber optics and associated electronics.

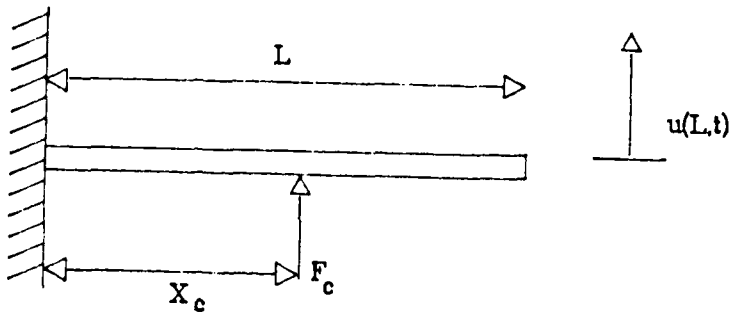

Fig. 4.2 The control force F_c is applied to the cantilever at x_c.

Using a beam with dimensions

L	=	11 in.
thickness	=	0.11 in.
width	=	3.0 in.

and

ρ	=	0.01848 lb.-in.
x_c	=	2.0 in.
EI	=	5228.1 lb.- $in.^2$,

and

F_o = 1.0 lb.

the following gains (K_n) were obtained

N	Kn
1	3.0687×10^{-1}
2	1.1031
3	7.2080×10^{-1}
4	-5.4712×10^{-1}
5	-15.6069

With this design, the controller will attempt to regulate only the position of the beam-tip. Even in the first mode of vibration, the deflection at the mid-span of the beam will generally not be zero, and if other modes are being excited, then it is possible for the beam to have a highly irregular, oscillating shape and yet still have its tip position controlled adequately.

An alternative approach is to control the shape of the entire length of the beam (i.e., control the deflections at many points along the beam). Theoretically, this can be accomplished for a cantilevered beam by using only one actuator (forcing device)[1], although any mode having a node at the actuator location cannot be controlled. To increase reliability, redundant actuators would be employed, and located at different positions. Fig. 4.3 is a block diagram for a multiposition regulator (i.e., one that controls the deflections at numerous points along the beam).

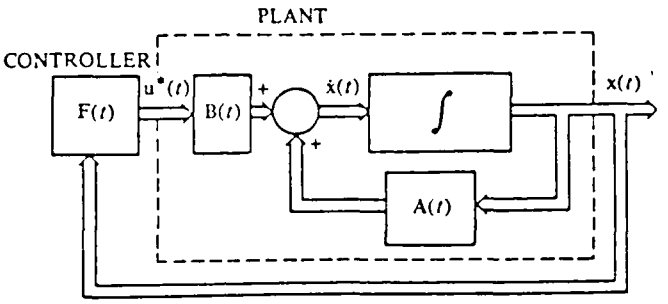

Fig. 4.3 The block diagram describes a multiposition regulator.[2]

The "plant" is the structure being controlled, and x is a vector of state variables (in this case, the deflections at specified points in the system). The matrices A and B are functions of the natural system dynamics, and can be identified from the output of a finite element model analysis. The vector u* is the optimal input (or set of inputs) from the controller [force(s) and/or moment(s)], optimal in that the overall deviation of the structural shape from nominal is minimized in some sense. Conceptually, the matrix function F could contain the necessary processing of the fiber output that is sensing the deflections (components of x).

By taking differences in integrated strains in the fibers, some of the noise in the sensing loop can be removed. Work in Phase II would explore how this differential strain information might be used in refining the single-fiber measurements.

---

1. It is also possible to augment the actuator system with torquing devices, such as gyroscopic reaction wheels, that exert internal moments on the structure.

2. Figure taken from Kirk, Optimal Control Theory.

4.3 General Case Using Embedded Fiber Sensor

A real space structure consists of complicated geometric shapes that defy straightforward analysis. In this situation, a finite element model can be developed and analyzed numerically (via NASTRAN, etc.) to get the characteristic frequencies and mode shapes. In principle, the signal from a single optical fiber embedded in a member would provide all the information necessary to effect the control. This information is obtained via a spectral decomposition of the fiber signal, giving the characteristic frequencies of vibration and their amplitudes. A prior calibration of these against the numerical analysis would allow determination of the shape of the member. It is that information that must be sensed and fed back in the control loop.

The implication of using a single fiber to sense the state of the system (i.e., the structural shape) is profound. Using multiple fibers would not only add robustness to the system by achieving redundancy, but would also introduce the possibility of determining differential strains (i.e., the strain occurring in a small section of the member between two loops) as shown below (Figure 4.4).

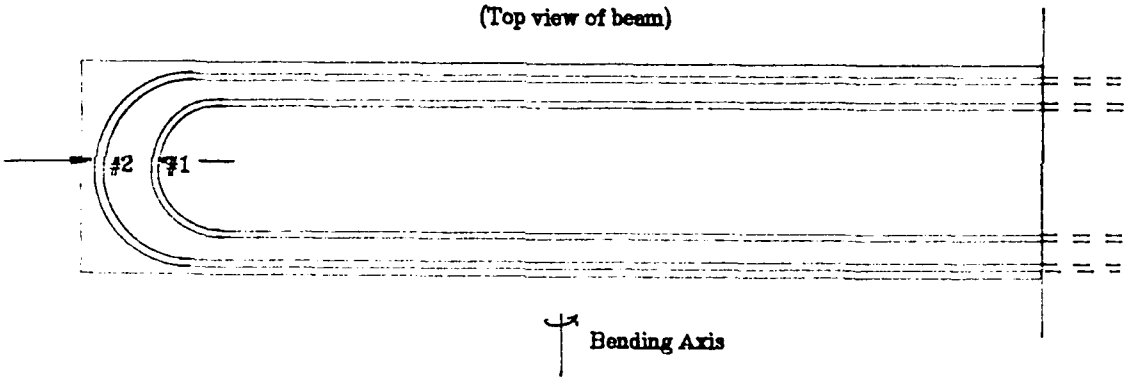

Figure 4.4 Differential strain in beam between arrows could be measured by subtracting integrated strain in fiber number 2 from that in number 1.

5. SUMMARY AND PHASE II DEVELOPMENT REQUIREMENTS

The objectives of Phase I, as repeated below, have been met:

- A baseline fabrication technique for composite-embedded fiber optic sensors was developed and a proof-of-principle configuration of fiber geometry were built.
- A broadband, wide dynamic range fiber interferometer that is robust and reliable was designed and tested.
- Vibration tests were performed at DTI and PSU to characterize sensor response and validate the theoretical model for an embedded sensor.
- Candidate control system architectures were identified which are consistent with the fundamental signal characteristics provided by a distributed fiber optic strain sensor.

These results provide a proof of the embedded sensor concept and a foundation for establishing the Phase II prototype development goals and requirements. Phase II requirements may be grouped into four areas:

Sensor Development

Embedded fiber sensor configurations should be refined to provide enhanced response in frequency ranges and bending modes likely to dominate the motion of real engineering structural elements (e.g. combined bending and torsion, differential strain, higher frequencies, etc.). The fabrication techniques should be refined to assure structural integrity of the element and facilitate large pieces. In this regard, the focussed SBIR effort can benefit from parallel programs in other agencies (e.g. Air Force, where material properties of embedded fiber sensors for aircraft components are being systematically assessed).

Subsystem Design

Common subgroups of structural elements can perhaps be linked together (either optically or through special software routines) to provide basic "building blocks" which can ultimately be combined in a much larger structure in a flexible and systematic fashion. In the long term, optical preprocessing of the raw interferometer output from such structural subgroups may substantially improve system efficiency. Closely related to this issue is the broad topic of fiber optic sensor multiplexing, which is receiving attention in a variety of sensor application areas. This related work will also benefit Phase II and full scale development.

Algorithm Implementation

The fundamental issues related to a control system matched to a distribution fiber sensor system have been evaluated in Phase I and candidate approaches have been identified. In Phase II specific algorithms should be written and tested in a small scale structure.

Subscale Testing

A small testbed should be constructed to perform an end-to-end validation the system design concepts developed in Phase II. The testbed will be efficient and flexible enough to permit an assessment of a variety of configurations under a realistic range of loading conditions. It is anticipated that much of the equipment can be drawn from the existing structural test facility at the Pennsylvania State University laboratory.

The success of Phase I and the continuing importance of space structure control for future programs suggest that extension of the current work into Phase II prototype development is a valuable investment.

REFERENCES

1. Roark, R. J., and Young, W. C., Formulas For Stress and Strain, McGraw-Hill, Inc., 1975, pg. 576.

2. Thomson, W. T., Theory of Vibration With Applications, Prentice-Hall, Inc., 1981, pp 218-21.

3. Giallorenzi, T. G., Bucaro, J. A., Dandridge, G. H. Cole, J. H., Rashleigh, S. C., and Preist, R. G., "Optical Fiber Sensor Technology," IEEE Transactions on Microwave Theory and Applications, Vol. MTT-30, No. 4, Apr 1982, pp 472-509.

4. Claus, R. O., and Wade, J. C., "Distributed Strain Measurement in a Rectangular Plate Using an Array of Optical Fiber Sensors," Journal of Nondestructive Evaluation, Vol. 4, No. 1, 1984, pp 23-27.

5. Butter, C. D., and Hocker, G. B., "Fiber Optics Strain Gauge," Applied Optics, Vol. 17, No. 18, September 1978, pp 2867-2869.

APPENDIX A

FIBER OPTIC VIBRATION SENSOR DATA

Plots of the sensor output signal and the vibration input signal at the first five resonant frequencies are contained in the appendix. The composite element was arranged as a cantilever of length 10.5 inches. The vibration peaks, as measured by the sensor, occurred at 29 Hz, 187 Hz, 290 Hz, and 578 Hz.

The second experiment consisted of exciting the cantilever with an impulse, and measuring the response. The upper trace is the response to the lower trace, which is the impulse. A spectrum is computed of the impulse response to determine the energy of the existing vibration modes.

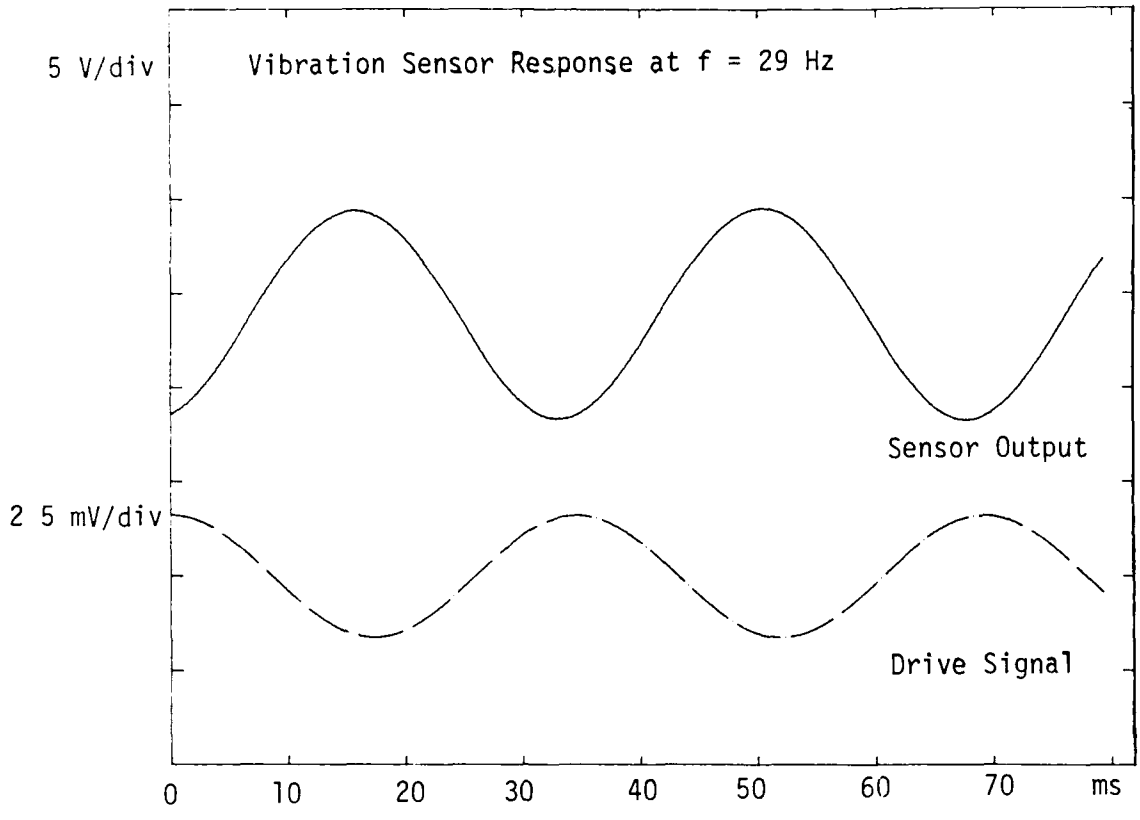
5 V/div
Vibration Sensor Response at f = 29 Hz
Sensor Output
2 5 mV/div
Drive Signal
0
10
20
30
40
50
60
70
ms

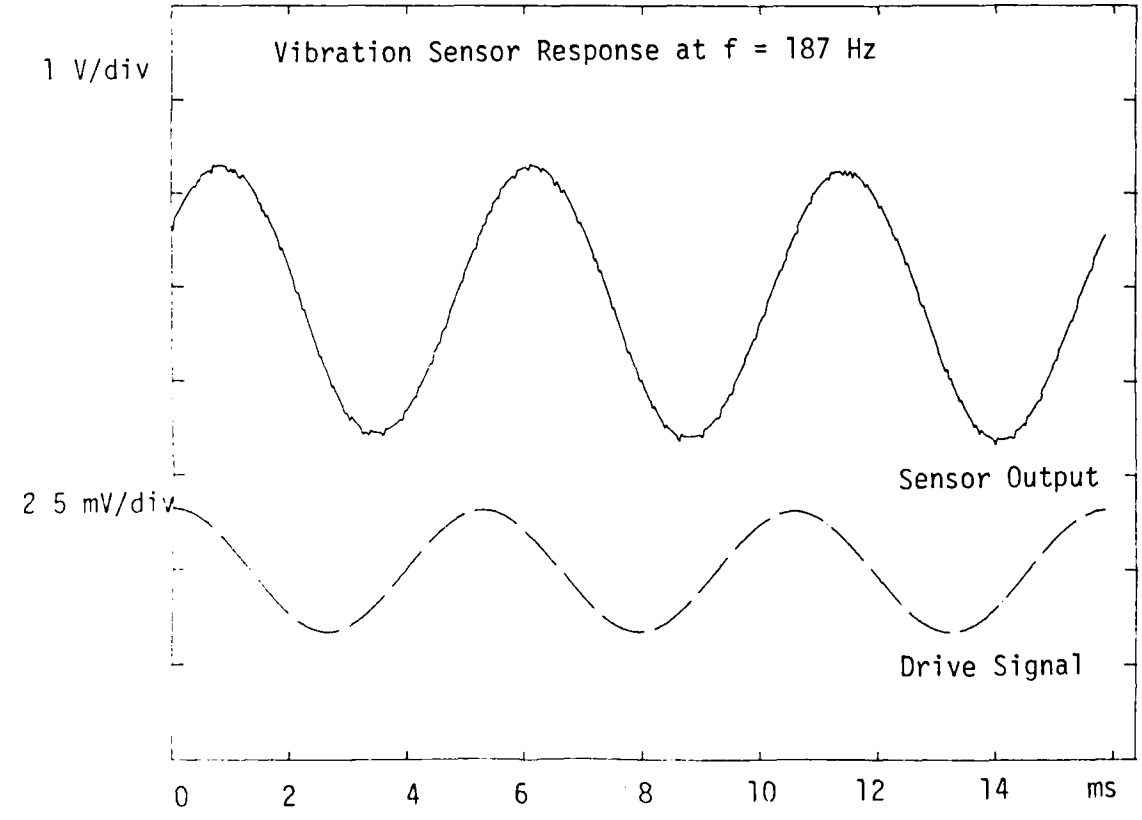
1 V/div
Vibration Sensor Response at f = 187 Hz
Sensor Output
2 5 mV/div
Drive Signal
0
2
4
6
8
10
12
14
ms

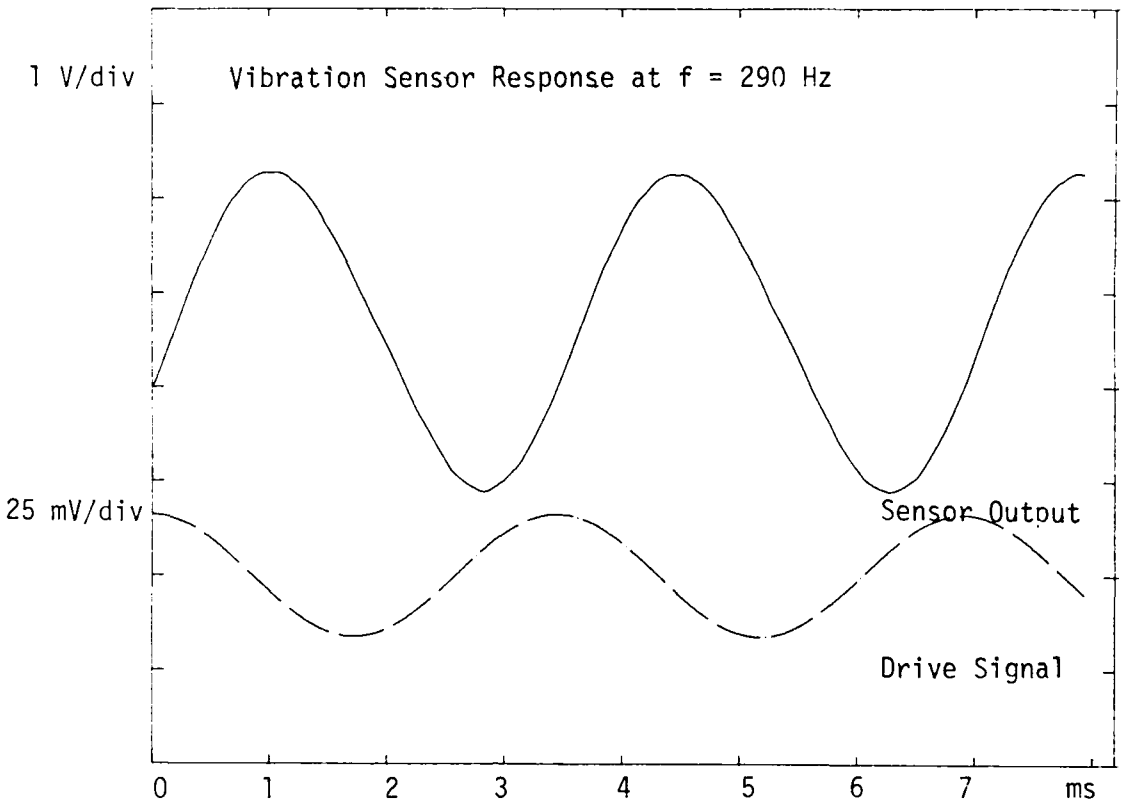
1 V/div
Vibration Sensor Response at f = 290 Hz
25 mV/div
Sensor Output
Drive Signal
0
1
2
3
4
5
6
7
ms

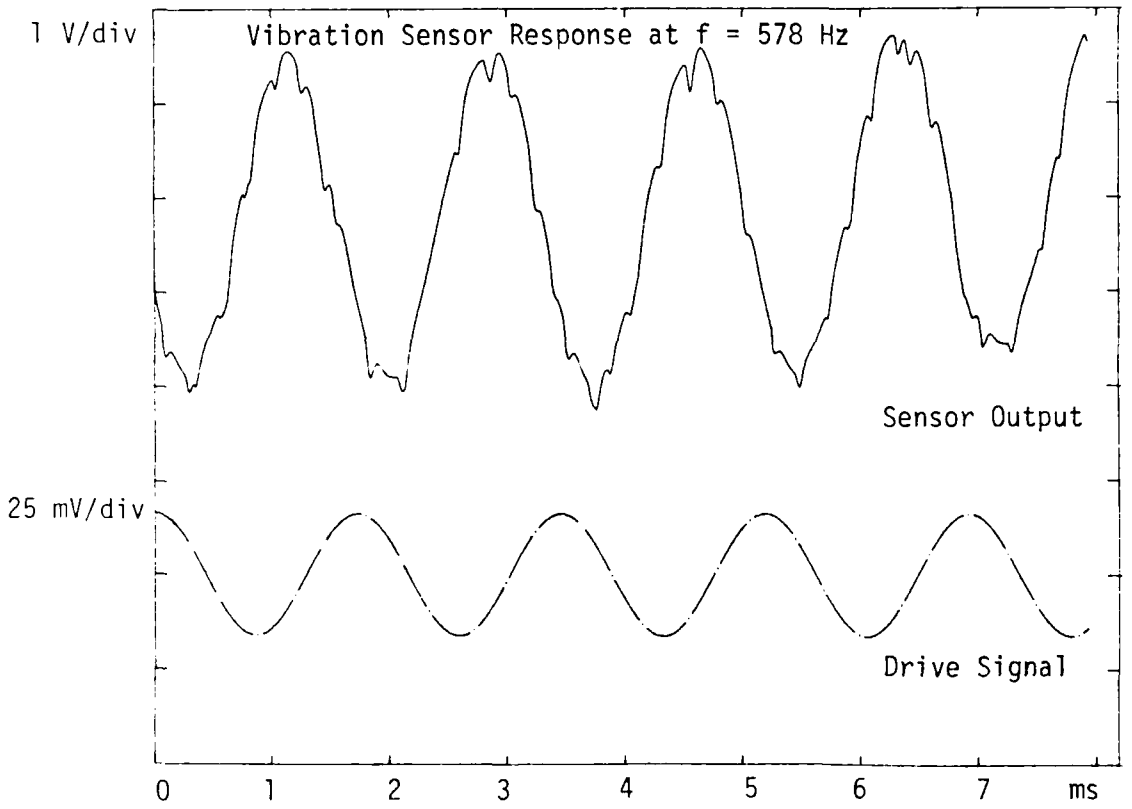
1 V/div
Vibration Sensor Response at f = 578 Hz
Sensor Output
25 mV/div
Drive Signal
0
1
2
3
4
5
6
7
ms

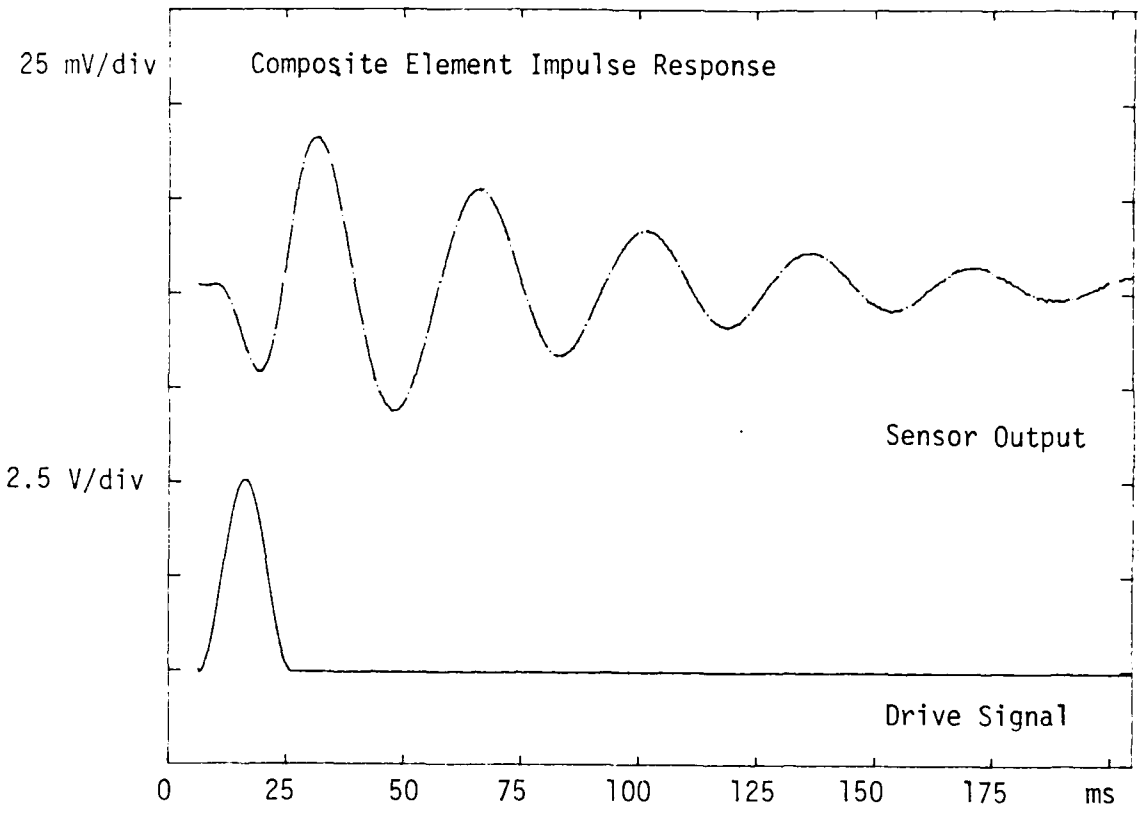
25 mV/div
Composite Element Impulse Response
Sensor Output
2.5 V/div
Drive Signal
0
25
50
75
100
125
150
175
ms

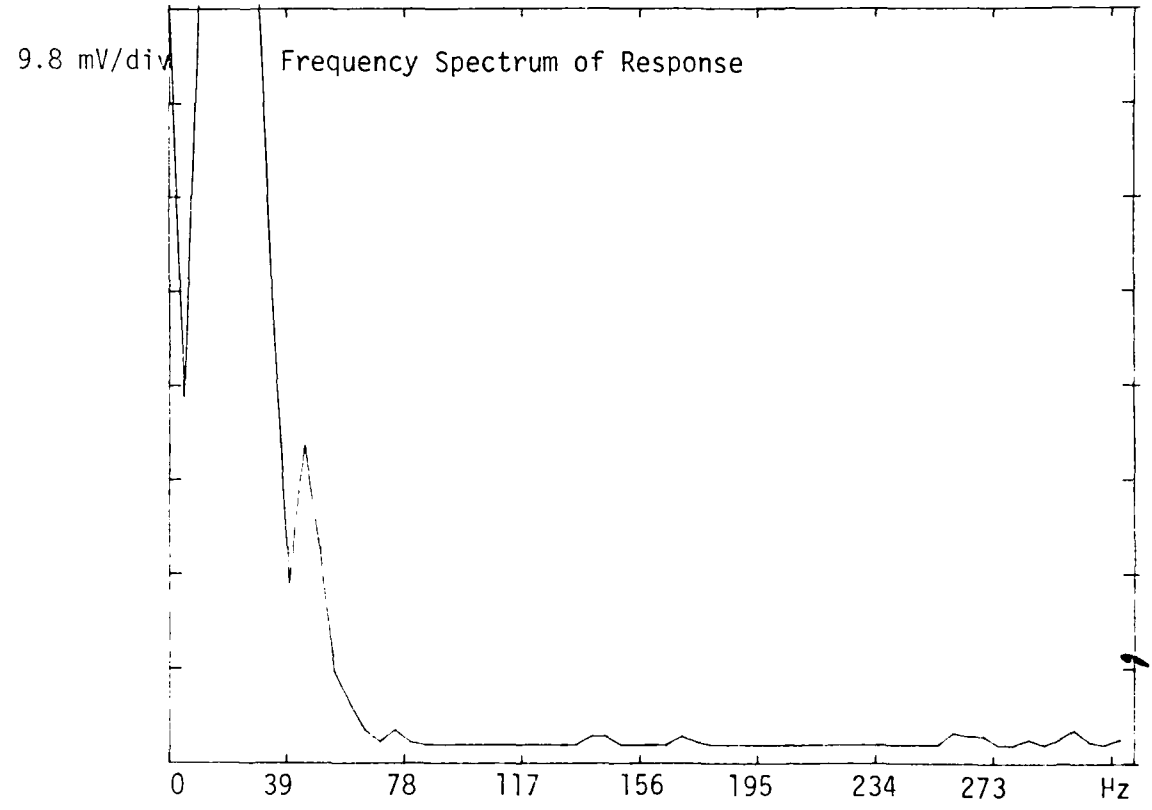
9.8 mV/div
Frequency Spectrum of Response
0
39
78
117
156
195
234
273
Hz

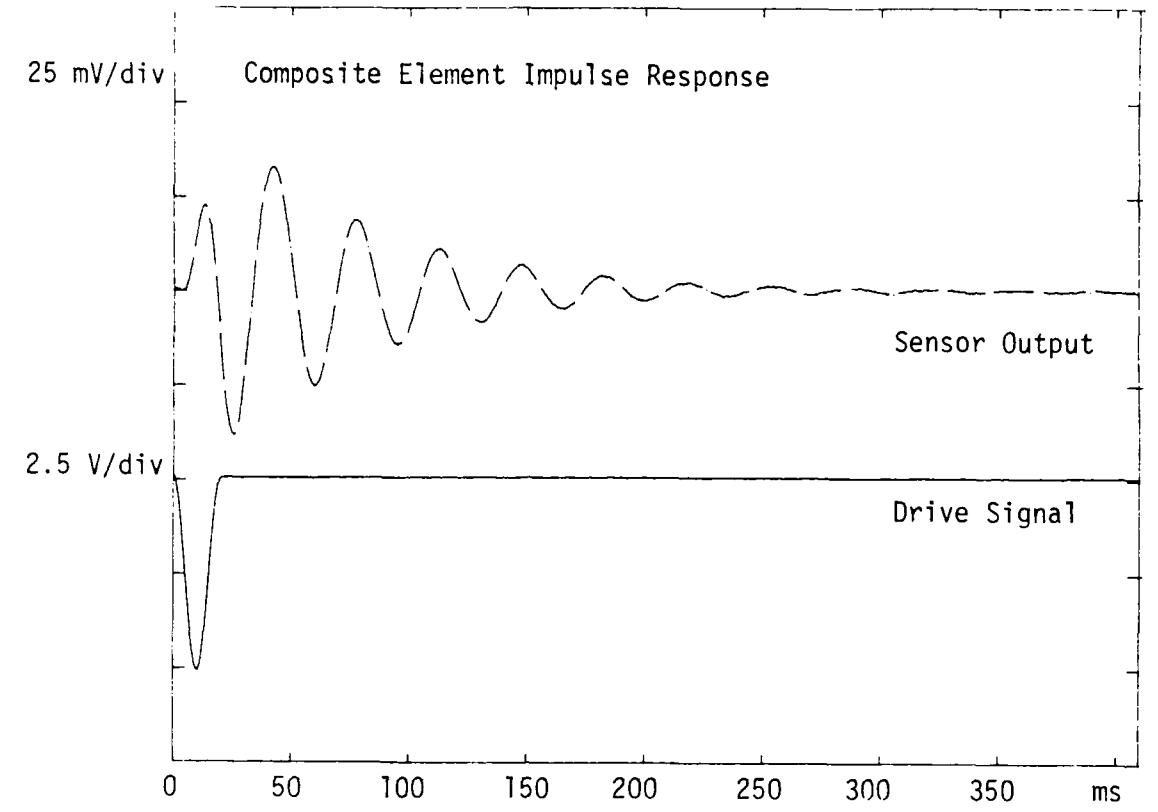
25 mV/div
Composite Element Impulse Response
Sensor Output
2.5 V/div
Drive Signal
0
50
100
150
200
250
300
350
ms

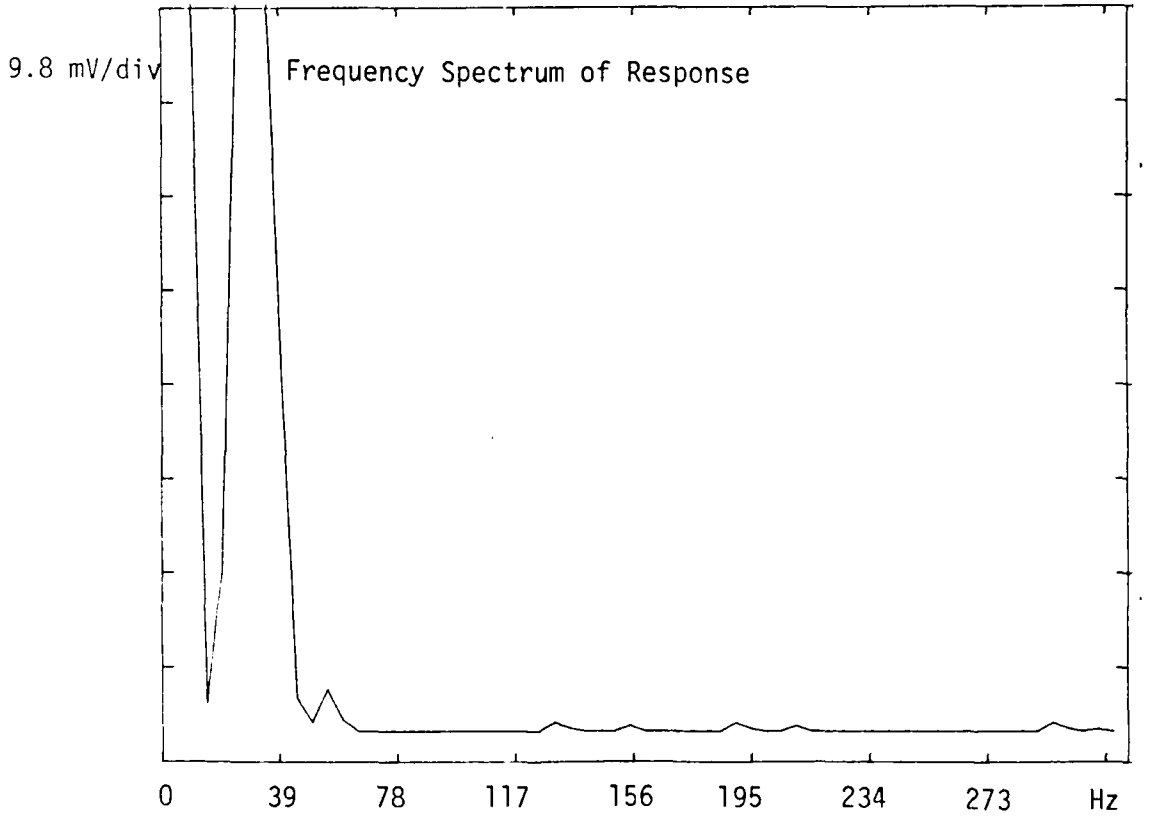
9.8 mV/div
Frequency Spectrum of Response
0
39
78
117
156
195
234
273
Hz

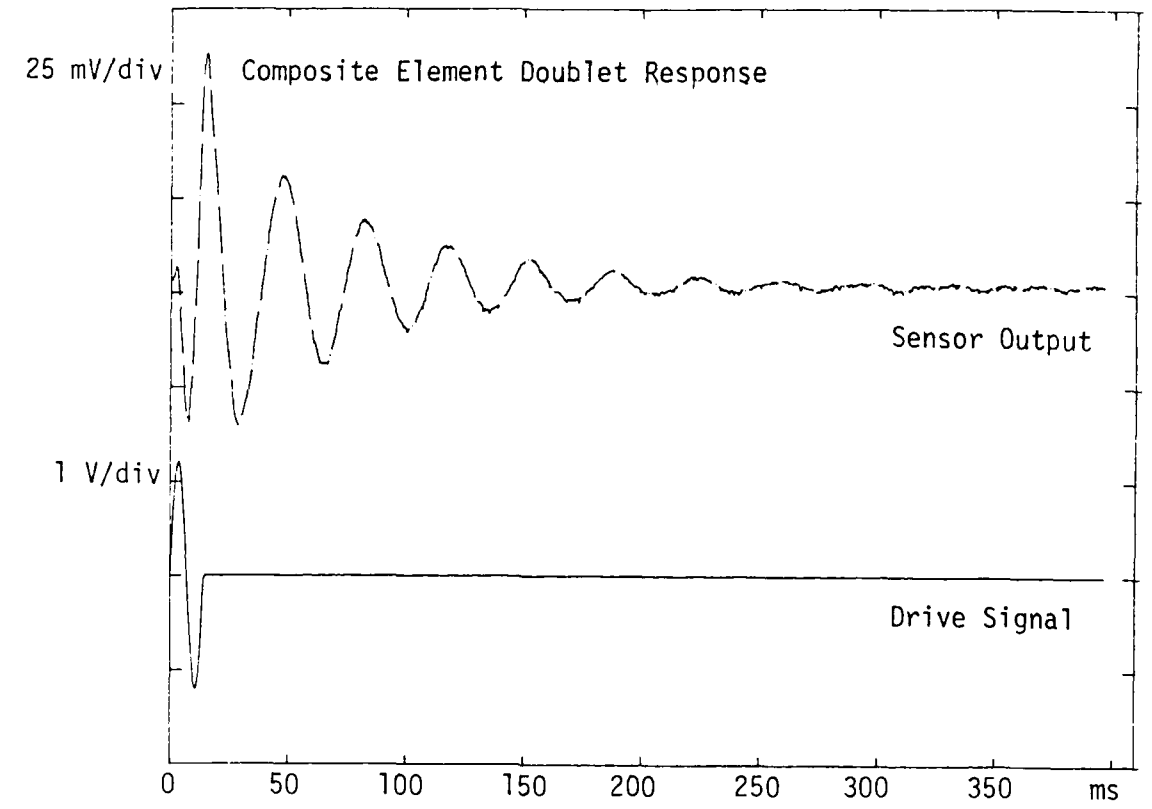
25 mV/div
Composite Element Doublet Response
Sensor Output
1 V/div
Drive Signal
0
50
100
150
200
250
300
350
ms

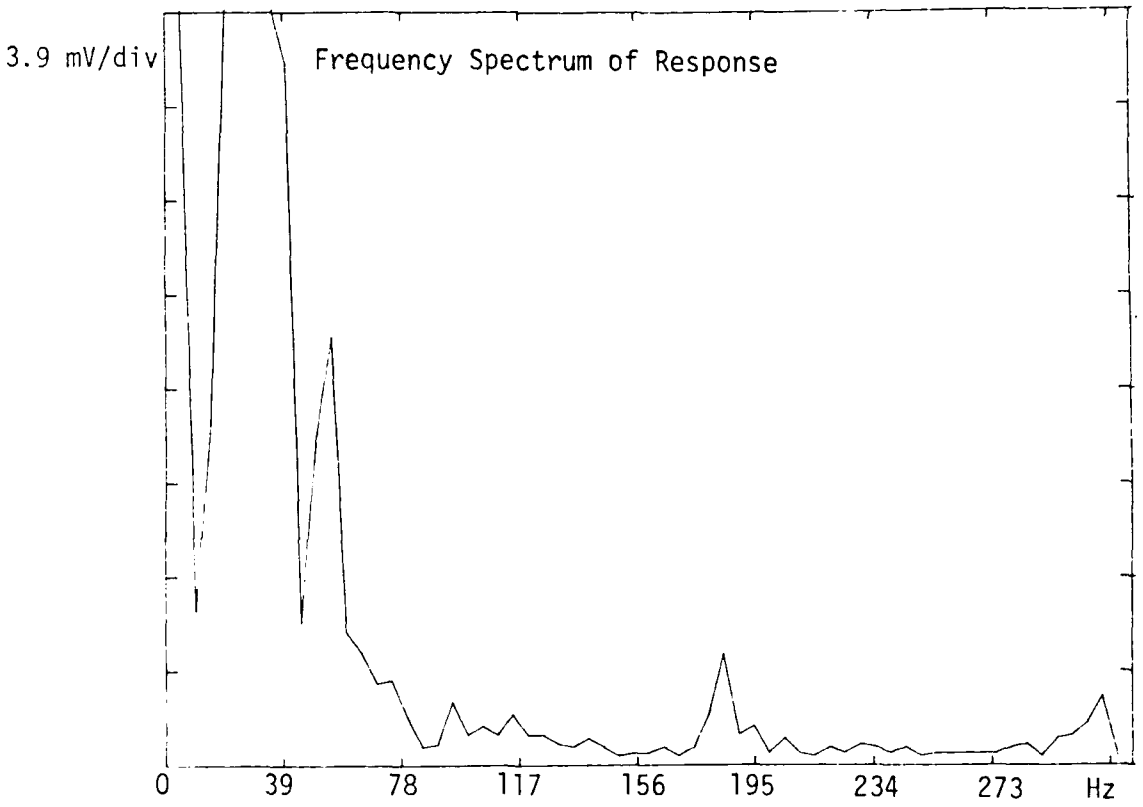
3.9 mV/div
Frequency Spectrum of Response
0
39
78
117
156
195
234
273
Hz

APPENDIX B

VIBRATION ANALYSIS OF THE CANTILEVER BEAM

The equation of motion for the lateral vibration of a beam can be found by examining the forces and moments acting on an element of the beam, as shown in Figure B1. The quantities involved are the shear moments V, bending moments M, and beam load per unit length p(x).

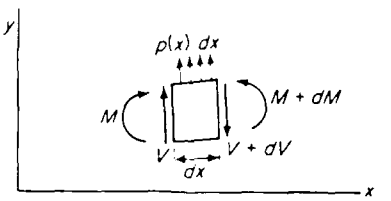

Figure B1.

The sum of the forces in the y direction gives the result,

$$dV - p(x)dx = 0 \tag{B1}$$

and the sum of the moments about any point on the right face of the element suggests,

$$dM - Vdx - \frac{1}{2} p(x) \ (dx)^2 = 0 \tag{B2}$$

These equations result in the following relationships,

$$dV/dx = p(x)$$

$$dM/dx = V \tag{B3}$$

Eqn. (B1) states that the rate of change of shear along the length of the beam is equal to the loading per unit length, and Eqn (B2) states the the rate of change of the moment along the beam is equal to the shear.

The bending moment M is related to the curvature by the flexure equation,

$$M = EI \ d^2u/dx^2 \tag{B4}$$

where E is the modulus of elasticity and I is the moment of inertia of the beam. Combining Eqns. B3 and B4 results in the lateral vibrational equation of motion:

$$\frac{d^2}{dx^2}\left[EI\frac{d^2u}{dx^2}\right] = p(x) \tag{B5}$$

The equation of motion, (B5), can be solved by use of a separation of variables technique, where the solution is assumed to be the product of a time dependent variable and a space dependent variable. Since the cantilever beam vibrates about its static equilibrium point, the load per unit length is equal to the inertial load due to its mass and acceleration. Since the inertial force is in the same direction as p(x), as shown in Fig. B1, the load can be said to oscillate with harmonic motion at frequency ω so that

$$p(x) = \rho\omega^2 u \tag{B6}$$

where ρ is the mass per unit length of the beam. The equation for the lateral vibration of the beam reduces to

$$\frac{d^2}{dx^2}\left[EI\frac{d^2u}{dx^2}\right] - \rho\omega u^2 = 0 \tag{B7}$$

For the present configuration, the flexural rigidity of the composite, EI, is assumed to be constant, and Eqn. (B7) can be written as

$$EI\frac{d^4u}{dx^4} - \rho\omega^2 u = 0 \tag{B8}$$

By denoting the following,

$$\beta^4 = \rho\omega^2/EI \tag{B9}$$

the fourth-order differential equation results:

$$\frac{d^4u}{dx^4} - \beta^4 u = 0 \tag{B10}$$

The general solution of Eqn. (B10) is given by

$$u(x) = A\cosh\beta x + B\sinh\beta x + C\cos\beta x + D\sin\beta x \tag{B11}$$

The boundary conditions of the cantilever are given by 0

$$\text{at } x=0 \begin{cases} u=0 \\ du/dx = 0 \end{cases}$$

$$\text{at } x=l \begin{cases} d^2u/dx^2 = 0 \\ d^3y/dx^3 = 0 \end{cases} \qquad \text{(B12)}$$

Substituting the boundary conditions in the general solution results

$$u(x)\Big|_{x=o} = A + C = 0 \Rightarrow A = -C$$

$$\frac{du}{dx}\Big|_{x=o} = \beta[A\sinh\beta x + B\cosh\beta x - C\sin\beta x + D\cos\beta x] = 0 \Rightarrow B = -D$$

$$\frac{d^2u}{dx^2}\Big|_{x=L} = o \Rightarrow A(\cosh\beta L + \cos\beta L) + B(\sinh\beta L + \sin\beta L = 0 \qquad \text{(B13)}$$

$$\frac{d^3u}{dx^3}\Big|_{x=L} = o \Rightarrow A(\sinh\beta L - \sin\beta L) + B(\cosh\beta L + \cos\beta L) = 0 \qquad \text{(B14)}$$

Dividing Eqn. (B13) by Eqn. (B14) reduces to the following,

$$\cosh(\beta L)\cos(\beta L) + 1 = 0 \qquad \text{(B15)}$$

A numerical method is required to solve Eqn. (B15) to determine the normal modes of oscillation. A Fortran program implementing the Newton routine has been used to solve for the roots of the equation, and the first twelve solutions are found in Appendix D.

Using Eqn. C9, the natural frequencies and the nodal positions for the first five modes have been listed in Table 1.

Mode	Angular Frequency	Nodal Position x/L
1	$w_1 = \frac{3.52}{L^2}\sqrt{\frac{EI}{\rho}}$	0.0
2	$w_2 = \frac{22.0}{L^2}\sqrt{\frac{EI}{\rho}}$	0.0 0.783
3	$w_2 = \frac{61.7}{L^2}\sqrt{\frac{EI}{\rho}}$	0.0 0.504 0.868
4	$w_2 = \frac{121}{L^2}\sqrt{\frac{EI}{\rho}}$	0.0 0.358 0.644 0.905
5	$w_2 = \frac{200}{L^2}\sqrt{\frac{EI}{\rho}}$	0.0 0.279 0.500 0.723 0.926

There are an infinite number of roots to Eqn. (B15), thus the general solution to (B10) can be written as a Fourier sum.

$$y(x,t) = \sum_{n=L}^{\infty} (A\cosh\beta_n x + B\sinh\beta_n x + C\cos\beta_n x + D\sin\beta_n x)\ E\sin W_n t + F\cos W_n t) \tag{B16}$$

APPENDIX C

SCHEMATICS OF THE ELECTRONIC FEEDBACK CIRCUITRY

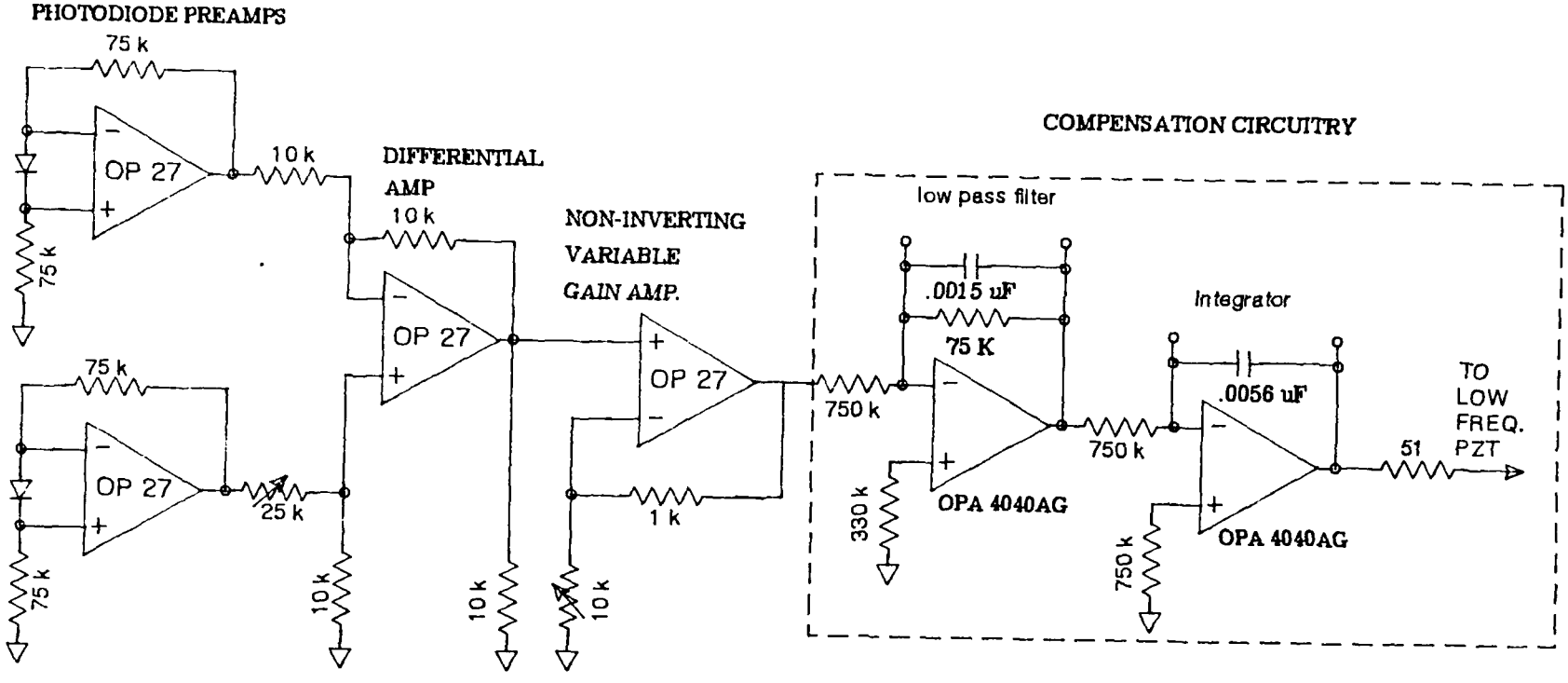

OPTICAL CONTROL CIRCUITRY
FOR TEST BED INTERFEROMETER

DRAWN BY: REV. # 1

APPROVED BY: DATE: 2-23-88

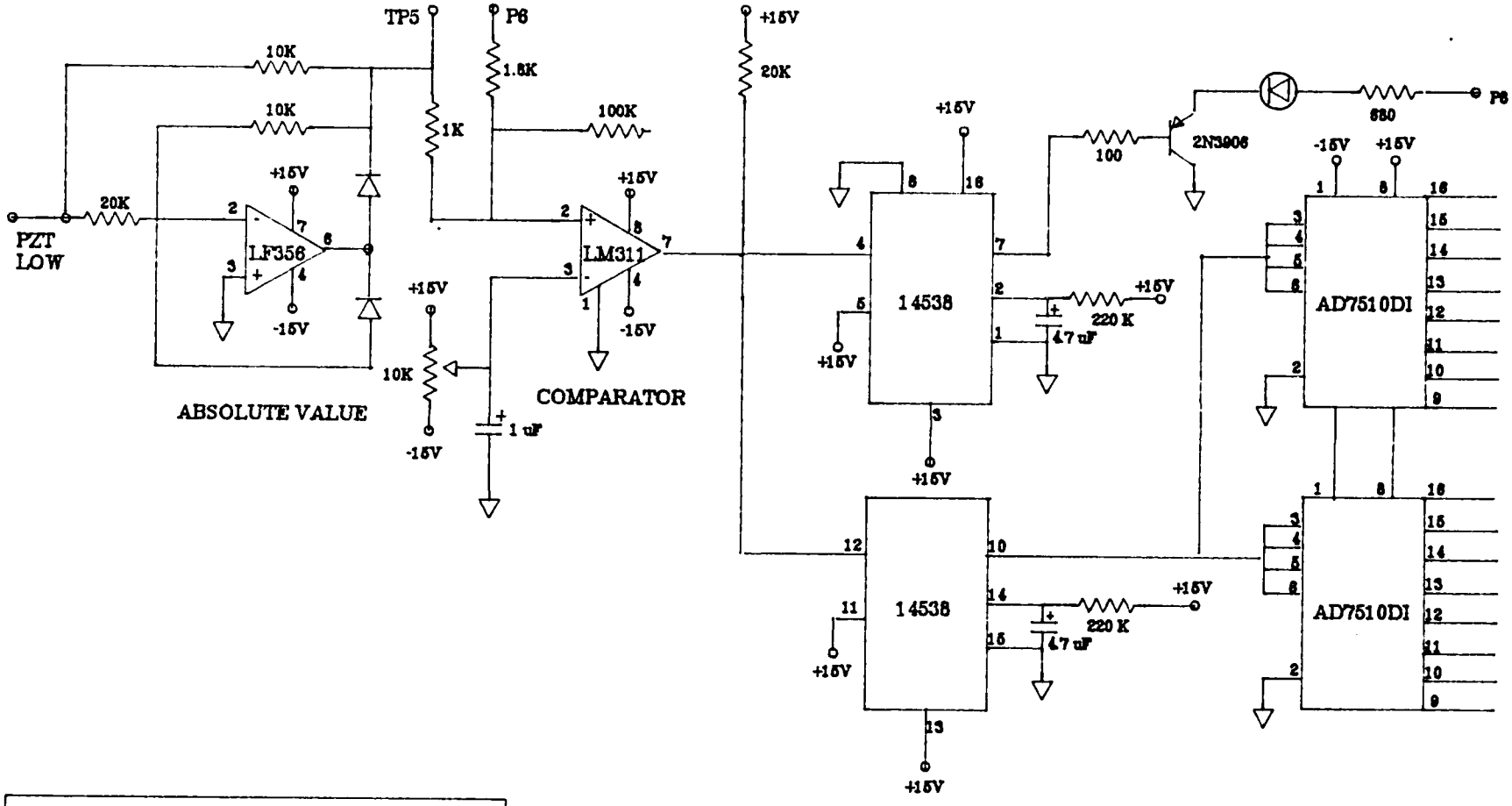

OPTICAL RESET CIRCUITRY

DRAWN BY: REV. #

APPROVED BY: DATE:

APPENDIX D

CALCULATION OF NATURAL FREQUENCIES OF CANTILEVER

The equation of motion of a cantilever beam has been derived and solved in Appendix B. The boundary equations are imposed to determine the natural frequencies of vibration. The resulting characteristic equation is found to be as follows:

$$\cosh(\beta L)\cos(\beta L) + 1 = 0$$

The roots of this equation are found by using a Newton method which takes a initial guess and iterates until the convergence conditions are met.

The first twelve natural frequencies found by this method are given below.

Mode	Frequency $(\beta_n)^2$
1	3.52
2	22.0
3	61.7
4	121
5	200
6	299
7	417
8	555
9	713
10	891
11	1088
12	1305